Title

Dynein/dynactin is necessary for anterograde transport of Mbp mRNA in oligodendrocytes and for myelination in vivo

Journal

Proceedings of the National Academy of Sciences of the United States of America, 114(43)

ISSN

0027-8424

Authors

Herbert, Amy L
Fu, Meng-Meng
Drerup, Catherine M
et al.

Publication Date

2017-10-24

DOI

10.1073/pnas.1711088114

Peer reviewed

PNAS PLUS

Dynein/dynactin is necessary for anterograde transport of *Mbp* mRNA in oligodendrocytes and for myelination in vivo

Amy L. Herbert[a,1], Meng-meng Fu[b,1,2], Catherine M. Drerup[c,3], Ryan S. Gray[a,4], Breanne L. Harty[a,5], Sarah D. Ackerman[a,6], Thomas O'Reilly-Pol[d], Stephen L. Johnson[d], Alex V. Nechiporuk[c], Ben A. Barres[b,2], and Kelly R. Monk[a,2,5]

[a]Department of Developmental Biology, Washington University School of Medicine, St. Louis, MO 63110; [b]Department of Neurobiology, Stanford University School of Medicine, Stanford, CA 94305; [c]Department of Cell, Developmental & Cancer Biology, Oregon Health and Science University, Portland, OR 97239; and [d]Department of Genetics, Washington University School of Medicine, St. Louis, MO 63110

Contributed by Ben A. Barres, August 25, 2017 (sent for review February 26, 2017; reviewed by Bruce Appel, Roman J. Giger, and Jeffery L. Twiss)

Oligodendrocytes in the central nervous system produce myelin, a lipid-rich, multilamellar sheath that surrounds axons and promotes the rapid propagation of action potentials. A critical component of myelin is myelin basic protein (MBP), expression of which requires anterograde mRNA transport followed by local translation at the developing myelin sheath. Although the anterograde motor kinesin KIF1B is involved in *mbp* mRNA transport in zebrafish, it is not entirely clear how *mbp* transport is regulated. From a forward genetic screen for myelination defects in zebrafish, we identified a mutation in *actr10*, which encodes the Arp11 subunit of dynactin, a critical activator of the retrograde motor dynein. Both the *actr10* mutation and pharmacological dynein inhibition in zebrafish result in failure to properly distribute *mbp* mRNA in oligodendrocytes, indicating a paradoxical role for the retrograde dynein/dynactin complex in anterograde *mbp* mRNA transport. To address the molecular mechanism underlying this observation, we biochemically isolated reporter-tagged *Mbp* mRNA granules from primary cultured mammalian oligodendrocytes to show that they indeed associate with the retrograde motor complex. Next, we used live-cell imaging to show that acute pharmacological dynein inhibition quickly arrests *Mbp* mRNA transport in both directions. Chronic pharmacological dynein inhibition also abrogates *Mbp* mRNA distribution and dramatically decreases MBP protein levels. Thus, these cell culture and whole animal studies demonstrate a role for the retrograde dynein/dynactin motor complex in anterograde *mbp* mRNA transport and myelination in vivo.

myelination | oligodendrocytes | dynactin | mRNA transport | dynein

In the central nervous system (CNS), specialized glial cells called oligodendrocytes wrap axons in many layers of plasma membrane to form the myelin sheath. Oligodendrocytes originate from neuroepithelial precursors that develop into oligodendrocyte precursor cells (OPCs), which are migratory and proliferative, extending numerous processes to sample the environment (1). OPCs differentiate into postmitotic oligodendrocytes, which activate expression of mature myelin proteins and ensheathe multiple axon segments with loose membrane spirals that are eventually compacted to form a functional myelin sheath (2). Disruption of the myelin membrane can cause debilitating human conditions, including multiple sclerosis. However, although the clinical applications of myelin research are clear, molecular mechanisms regulating basic oligodendrocyte development are not well understood.

A critical protein generated during oligodendrocyte differentiation is myelin basic protein (MBP), which is essential for proper compaction of the myelin sheath. Due to its highly basic charge and propensity to promote membrane adherence, *Mbp* translation is tightly regulated during oligodendrocyte development (3). *Mbp* mRNA is trafficked to the developing sheath and translated locally (4, 5). Translation at the membrane and formation of myelin sheaths is stimulated by Fyn kinase, which is phosphorylated in response to axonal electrical activity (6–8). In addition, MBP acts as an important spatial and temporal regulator of myelination, by triggering disassembly of the actin cytoskeleton to promote initiation of myelin membrane wrapping (9, 10).

Classic experiments in cultured oligodendrocytes demonstrated that *Mbp* mRNA trafficking in the anterograde direction (away from the cell body) relies on microtubules (11). By electron microscopy, these microtubules are uniformly oriented with polymerizing plus ends directed away from the cell body (12). Two types of motors move along microtubules: a vast family of kinesin motors, the majority of which move toward the plus end, and a single cytoplasmic dynein motor that moves toward the

Significance

Oligodendrocytes in the brain insulate neuronal axons in layers of fatty myelin to facilitate fast electrical signaling. Myelin basic protein (MBP), an important myelin component, is transported as mRNA away from the cell body before being translated into protein. In zebrafish, the anterograde motor kinesin transports *mbp* mRNA away from the cell body. We now identify myelination defects in zebrafish caused by a mutation in the retrograde motor complex dynein/dynactin, which normally transports cargos back toward the cell body. However, this mutant displays defects in anterograde *mbp* mRNA transport. We confirm in mammalian oligodendrocyte cultures that drug inhibition of dynein arrests transport in both directions and decreases MBP protein levels. Thus, dynein/dynactin is paradoxically required for anterograde *mbp* mRNA transport.

Author contributions: A.L.H., M.-m.F., R.S.G., B.L.H., S.D.A., A.V.N., B.A.B., and K.R.M. designed research; A.L.H., M.-m.F., R.S.G., B.L.H., S.D.A., T.O.-P., and K.R.M. performed research; C.M.D., T.O.-P., S.L.J., and A.V.N. contributed new reagents/analytic tools; A.L.H., M.-m.F., C.M.D., R.S.G., B.L.H., S.D.A., T.O.-P., S.L.J., B.A.B., and K.R.M. analyzed data; and A.L.H., M.-m.F., C.M.D., S.L.J., A.V.N., B.A.B., and K.R.M. wrote the paper.

Reviewers: B.A., University of Colorado Medical School; R.J.G., University of Michigan; and J.L.T., University of South Carolina.

The authors declare no conflict of interest.

Freely available online through the PNAS open access option.

[1]A.L.H. and M.-m.F. contributed equally to this work.

[2]To whom correspondence may be addressed. Email: mengmengfu@gmail.com, barres@stanford.edu, or monk@ohsu.edu.

[3]Present address: National Institute of Child Health and Human Development, National Institutes of Health, Bethesda, MD 20892.

[4]Present address: Department of Pediatrics, Dell Medical School, University of Texas at Austin, Austin, TX 78723.

[5]Present address: Vollum Institute, Oregon Health and Science University, Portland, OR 97239.

[6]Present address: Institute of Neuroscience, University of Oregon, Eugene, OR 97403.

This article contains supporting information online at www.pnas.org/lookup/suppl/doi:10.1073/pnas.1711088114/-/DCSupplemental.

minus end when bound to the dynactin activator complex (13). Previously, a genetic screen in zebrafish identified a kinesin *kif1b* mutant in which anterograde *mbp* mRNA transport is disrupted, resulting in mislocalization of *mbp* mRNA in oligodendrocyte cell bodies (14). Importantly, another zebrafish genetic screen for myelination defects uncovered a dynein mutation that results in decreased *mbp* mRNA levels in both the peripheral nervous system (PNS) and CNS, highlighting the necessity of molecular motors in myelination (15, 16).

Classic transport studies have demonstrated the interdependence of oppositely directed motors. Many vesicular cargos are simultaneously associated with both dynein and kinesin motors, and inhibition or loss of either motor results in transport arrest in both anterograde and retrograde directions (17). This has been observed for organelles in squid axoplasm treated with anti-dynactin antibodies (18); for synaptic vesicles in axons of *Drosophila* with mutations in kinesin, dynein, or dynactin (19); and for vesicles and lysosomes in mammalian axons in which subunits of kinesin and dynactin have been knocked down (20, 21). Though less is known about how opposing motors regulate mRNA transport, one early study in *Drosophila* S2 macrophage-like cells showed that dynein knockdown leads to arrested transport in both anterograde and retrograde directions of fluorescently tagged fragile X mental retardation protein (FMRP), which is an RNA-binding protein (22). However, a role for the interdependence of kinesin and dynein motors in mRNA transport has yet to be shown in glial cells.

Here, we demonstrate in vivo in zebrafish and in mammalian oligodendrocyte cultures that dynein/dynactin is required for anterograde *mbp* mRNA transport. In a myelination screen in zebrafish, we discovered a mutation in a subunit of the dynein activator dynactin. This mutation in *actr10*, which encodes the Arp11 protein, results in dynein/dynactin loss-of-function phenotypes, such as photoreceptor loss and aberrant melanosome distribution in pigment cells. Mutants have OPC proliferation defects, fewer myelinated axons by transmission electron microscopy (TEM) and reduced levels of *mbp* mRNA, all of which phenocopy a previously published zebrafish dynein mutant (16). Interestingly, of the oligodendrocytes that are present in the mutants, we noticed a reduction in *mbp* mRNA localized to processes, which is similar to the previously published kinesin *kif1b* zebrafish mutant and therefore may be caused by mRNA transport defects (14). To test whether dynein/dynactin directly plays a role in *mbp* mRNA transport, we turned to primary rodent oligodendrocyte cultures. Coimmunoprecipitations demonstrated that *Mbp* mRNA granules indeed associate with dynactin and dynein. Furthermore, imaging of *Mbp* mRNA granules in primary oligodendrocytes revealed movement in the anterograde direction, as expected; unexpectedly, the granules also move transiently backward in the retrograde direction. To test how dynein activity affects *Mbp* mRNA transport, we pharmacologically inhibited dynein using ciliobrevin in both zebrafish larvae and cell culture. In zebrafish, ciliobrevin treatment reduced *mbp* mRNA localization in oligodendrocyte processes; in primary oligodendrocytes, this resulted in arrested transport in both anterograde and retrograde directions and also dramatically reduced MBP protein levels. Taken together, our cellular and in vivo data demonstrate a previously unappreciated role for dynein/dynactin in anterograde *Mbp* mRNA transport in developing oligodendrocytes.

Results

***actr10* Mutations in Zebrafish Cause Reduced *mbp* mRNA Levels.** To investigate the development of myelinated axons, we performed a large-scale *N*-ethyl-*N*-nitrosourea (ENU)-based forward genetic screen in which we visualized axons using the transgenic reporter *tg(llhx1a:GFP)* (23), then imaged myelin using *mbp* in situ hybridization (ISH). We uncovered a mutant, designated *stl83*, with both GFP-positive axonal swellings (Fig. 1 *A* and *B*) and reduced levels of *mbp* by ISH (Fig. 1 *C* and *D*). Whole genome sequencing of equimolar pools of mutants and siblings and subsequent analysis using an in-house pipeline (24) were used to determine that the gene of interest likely resided on chromosome 20 (Fig. 1*E*). Further single-nucleotide polymorphism (SNP) subtraction analysis to compare these data to other whole genome sequencing datasets reduced the number of candidate genes within our mapped locus to five, including one in *actr10* (Fig. 1*F*). To test if the *stl83* mutation was indeed in *actr10*, we performed a complementation test using a second *actr10* mutant allele ($actr10^{nl15}$) (25). While the putative $actr10^{stl83}$ allele results from a G-to-T transversion in exon 12, resulting in a glycine to tryptophan amino acid change, the $actr10^{nl15}$ allele is a putative null mutation in the start site of *actr10* (Fig. 1*G* and Fig. S1*A*). Complementation analysis confirmed that the *stl83* phenotype results from a mutation in *actr10,* as transheterozygous animals have axonal swellings, which are never seen in either heterozygous or wild-type (WT) animals from either genotype (Fig. 1 *H* and *I*). Although the $actr10^{stl83}$ mutation occurs late in the genomic sequence, both mutants are lethal at the larval stage. The $actr10^{stl83}$ mutants are grossly healthier than the $actr10^{nl15}$ mutants (Fig. S1*D*), indicating that $actr10^{stl83}$ may be a hypomorphic allele.

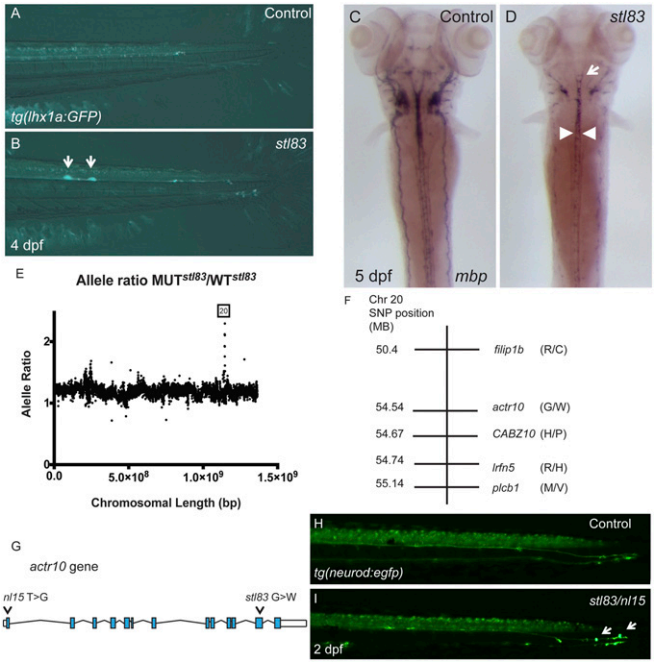

Fig. 1. A forward genetic screen uncovers *actr10* mutants. (*A*) *tg(lhx1a:gfp)* marks axons in the tail of a control zebrafish larva at 4 dpf. (*B*) *stl83* mutants exhibit axonal swellings in the CNS (arrows). (*C*) *mbp* ISH in a control animal at 5 dpf shows robust *mbp* mRNA levels. (*D*) An *stl83* mutant animal exhibits reduced *mbp* mRNA in the hindbrain (arrow) and spinal cord (arrowheads). (*E*) Analysis of whole genome sequencing data revealed a higher mutant-to-WT allele ratio on chromosome 20, and SNP subtraction analysis (*F*) narrowed the number of candidate genes to five. (*G*) Diagram of *actr10* genomic structure shows the location of the *nl15* mutation in exon 1 and the *stl83* mutation in exon 12. (*H*) In a *tg(neurod:egfp)* background, the lateral line is normal in the tail of control animals at 2 dpf. (*I*) A complementation cross demonstrated that transheterozygous *stl83/nl15* animals have axonal swellings in the PNS ($actr10^{stl83/nl15}$: $n = 22$) (arrows), which are never seen in either heterozygous or WT animals from either genotype ($actr10^{+/+}$: $n = 47$; $actr10^{stl83/+}$: $n = 13$; $actr10^{nl15/+}$: $n = 9$). *A*, *B*, *H*, and *I*, lateral views, dorsal up; *C* and *D*, dorsal views, anterior up. (Magnification: *A* and *B*, 80×; *C* and *D*, 50×; *H* and *I*, 160×.)

actr10 Mutants Have Fewer Myelinated Axons. To directly observe the ultrastructure of the myelin sheath, we performed TEM of both *actr10* mutant alleles and counted the number of myelinated axons in a hemisegment of the ventral spinal cord. Of note, heterozygous *actr10*$^{stl83/+}$ and *actr10*$^{nl15/+}$ animals are viable and have no discernable phenotype compared with WT siblings as assessed by *tg(neurod:egfp)* from the complementation cross and number of myelinated axons by TEM (Fig. S1 *E* and *F*) and are therefore combined with WT as "controls." Consistent with our *mbp* ISH analysis, both *actr10* mutant alleles have significantly fewer myelinated axons compared with control animals by TEM at 5 d postfertilization (dpf) (Fig. 2), demonstrating that dynein/dynactin dysfunction has functional consequences for myelin in the CNS.

actr10$^{nl15/nl15}$ Mutants Have Fewer OPCs. One explanation for reduced myelinated axon numbers in *actr10* mutants could be fewer OPCs. To test this, we examined spinal cord cross-sections from double transgenic *tg(olig2:dsred);tg(sox10:mgfp)* (26, 27) zebrafish to quantify OPC number in putative null *actr10*$^{nl15/nl15}$ mutants. *olig2* is expressed in OPCs and motor neurons at 3 dpf, *sox10* is expressed in OPCs, and the *tg(olig2:dsred);tg(sox10:mgfp)* transgenes combined allow for visualization of OPCs with red cytoplasm and green membrane. At 3 dpf, *actr10*$^{nl15/nl15}$ mutants had fewer OPCs compared with controls (Fig. 3 *A*–*C*), indicating a role for *actr10* in OPC development.

In the zebrafish spinal cord, OPCs originate ventrally and then migrate dorsally on either side of the neuronal cell bodies located in the center of the spinal cord (28). A population of OPCs remains in the ventral cord to differentiate and myelinate ventral axons, while the dorsally migrated OPCs differentiate and myelinate axons in the dorsal spinal cord. Dorsal OPCs can be visualized using the *tg(olig2:dsred)* transgene and are easily distinguished by their elongated cell bodies (Fig. 3 *D*–*E*') (28). Using this elongated cellular morphology as a metric, we found that the number of DsRed-positive elongated cells in the dorsal spinal cord was reduced at 3 dpf in *actr10*$^{nl15/nl15}$ mutants compared with controls (Fig. 3*F*). To determine whether this resulted from a delay in migration and maturation, we similarly assayed 4 dpf animals and also found a significant reduction at this later time point (Fig. 3*G*). Together, these data demonstrate that *actr10*$^{nl15/nl15}$ mutants have reduced numbers of OPCs and fewer dorsally migrated OPCs, recapitulating early defects described in zebrafish dynein mutants (16). Importantly, however, some maturing dorsal OPCs are present in *actr10*$^{nl15/nl15}$ mutants, indicating that migration defects alone are not the sole cause of the myelination phenotypes observed in mutants.

OPC Proliferation Is Slower in actr10$^{nl15/nl15}$ Mutants. Interestingly, depletion of Arp11 in mammalian COS7 resulted in the striking formation of multiple spindles during mitosis (29). To better understand the mechanistic role of Arp11 in OPC proliferation and cell division, we performed live imaging using the transgenic line *tg(nkx2.2a:megfp),* which also marks OPCs (1). Transgenic zebrafish were imaged for up to 12 h starting at ~57 h postfertilization (hpf). During this time period in oligodendrocyte development, OPCs have been specified and continue to divide and migrate from the ventral to the dorsal spinal cord. They continuously extend and retract exploratory processes to sample the environment before becoming postmitotic and beginning to myelinate (1). Live imaging revealed that mutant *nkx2.2a*-labeled cells took longer to divide compared with cells in control sibling *actr10*$^{nl15/+}$ animals (Fig. 4 and Movies S1–S4). During division, the *nkx2.2a*-labeled cells retract processes and become distinctly round before dividing. In the control animals, the time from beginning of rounding until division or the end of live imaging takes an average of 46 min, compared with 159 min in mutants,

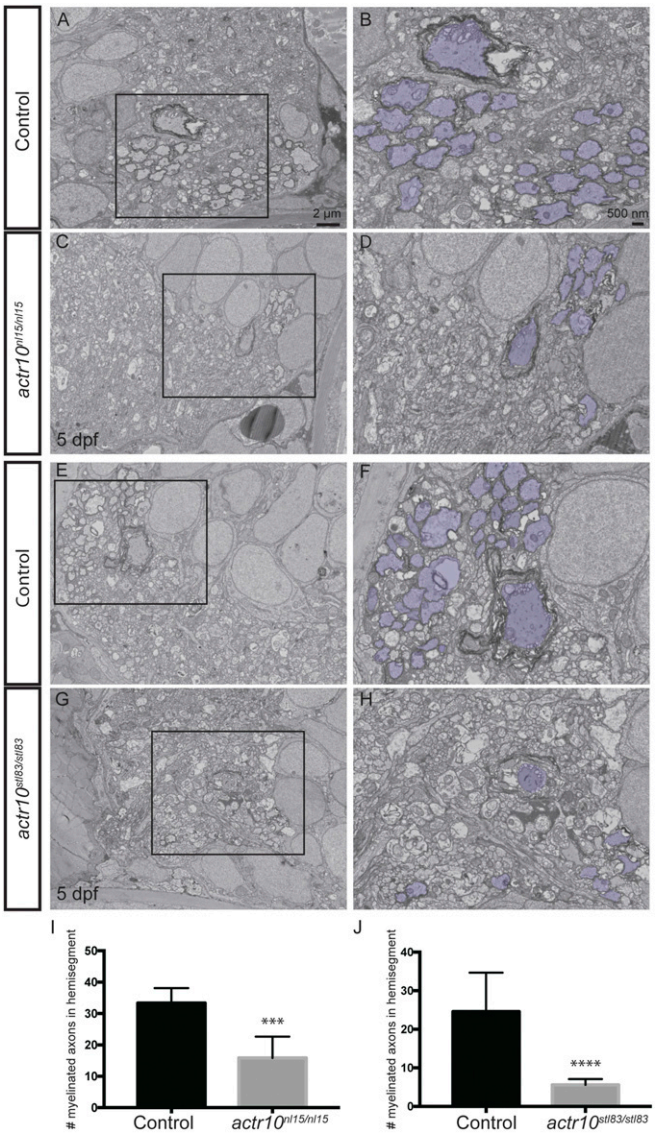

Fig. 2. *actr10* mutants have fewer myelinated axons in the ventral spinal cord. (*A*) Myelinated axons in a control larva in a hemisegment of the ventral spinal cord at 5 dpf. (*B*) Pseudocoloring and higher magnification enhance visualization of control myelinated axons. (*C* and *D*) Myelinated axons are similarly shown in a quadrant of the ventral spinal cord in an *actr10*$^{nl15/nl15}$ mutant animal. (*E* and *F*) Myelinated axons in a control larva in a quadrant of the ventral spinal cord at 5 dpf. (*G* and *H*) Myelinated axons are similarly shown in a quadrant of the ventral spinal cord in an *actr10*$^{stl83/stl83}$ mutant animal at 5 dpf. (*I* and *J*) Quantification revealed a significant difference in the number of myelinated axons in a ventral quadrant between control animals ($n = 6$) and *actr10*$^{nl15/nl15}$ mutants ($n = 4$; $^{***}P < 0.0006$) (*I*) and between control animals ($n = 8$) and *actr10*$^{stl83/stl83}$ mutants ($n = 5$; $^{****}P < 0.0001$) (*J*) at 5 dpf. Unpaired *t* tests with Welch's correction were used for statistical analysis.

suggesting that reduced OPC numbers are in part due to slower OPC proliferation.

Dynein Activity Is Impaired in Multiple Tissues in actr10$^{nl15/nl15}$ Mutants. Previous studies have found that loss of Arp11 disrupts the assembly of the dynactin complex in mammalian cell culture and in the filamentous fungi *Aspergillus nidulans* (29, 30). Actr10 has recently been shown to have a specific role in retrograde mitochondrial transport in peripheral axons without disrupting dynein/dynactin complex integrity (25). We hypothesized, however, that oligodendrocyte cell lineage and myelin phenotypes in *actr10*$^{nl15/nl15}$

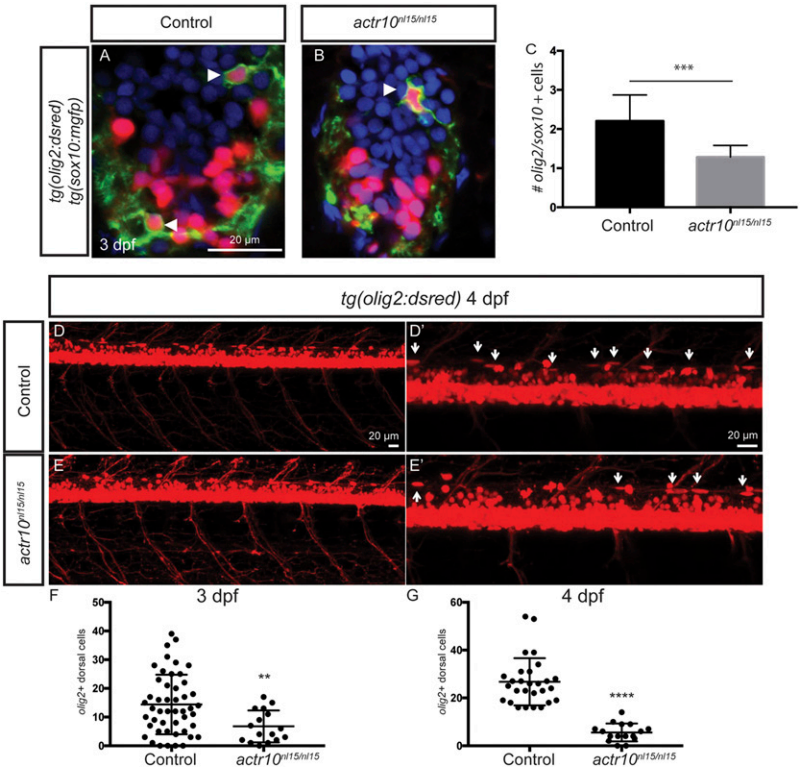

Fig. 3. *actr10*$^{nl15/nl15}$ mutants have fewer OPCs. (*A* and *B*) Double transgenic *tg(sox10:mgfp);tg(olig2:dsred)* larvae were used to identify OPCs in spinal cord cross-sections at 3 dpf. Arrowheads mark OPCs, which are labeled by cytoplasmic DsRed and membrane-tagged GFP. (*C*) Mutants ($n = 7$) have significantly fewer OPCs in the spinal cord compared with sibling controls ($n = 16$; ***$P < 0.0002$). (*D*–*G*) The *tg(olig2:dsred)* line was used to count the number of *olig2*-labeled elongated cells in control animals (*D* and *D*′, arrows) compared with *actr10*$^{nl15/nl15}$ mutants (*E* and *E*′, arrows) at 3 dpf and at 4 dpf (pictured). (*F*) Quantification revealed a significant difference between the number of *olig2*-labeled dorsal cells in controls ($n = 48$) compared with *actr10*$^{nl15/nl15}$ mutants ($n = 16$; **$P < 0.007$) at 3 dpf. (*G*) Similarly, there was also a significant difference between controls ($n = 28$) and *actr10*$^{nl15/nl15}$ mutants ($n = 16$; ****$P <$ 0.0001) at 4 dpf. Unpaired *t* tests with Welch's correction were used for statistical analysis.

mutants result from general disruption to dynein/dynactin function for several reasons. Firstly, mutants have defects in OPC development and myelination that are similar to those previously defined in zebrafish dynein mutants (16). Secondly, mutants phenocopy the photoreceptor loss observed in zebrafish with mutations in other subunits of dynactin, including *p150*^{Glued} and *p50* (31–33) (Fig. S2 *A* and *B*). The photoreceptor defects observed indicated that the fish might be blind. To this end, we used the Noldus behavior unit, DanioVision, to assay the response of WT, *actr10*$^{nl15/+}$, and *actr10*$^{nl15/nl15}$ animals during light/dark cycles. Larval zebrafish, unlike their adult counterparts, avoid the dark and respond with increased movement (34, 35). The movement of larvae in a 96-well plate was tracked during an alternating light/dark cycle. Both WT (Fig. S2*G*) and *actr10*$^{nl15/+}$ animals (Het) (Fig. S2*H*) showed a significant increase in movement in the dark compared with the light. However, *actr10*$^{nl15/nl15}$ animals (Mut) showed no significant difference in movement between the light baseline and dark response (Fig. S2*I*), indicating that the observed photoreceptor death likely leads to blindness.

Thirdly, *actr10*$^{nl15/nl15}$ animals phenocopy the excessive pigment observed in the dorsal head region of zebrafish dynein mutants (16) (Fig. S2 *C* and *D*) and also have increased pigment along the lateral line (Fig. S2 *E* and *F*). Interestingly, blindness has been shown to cause background adaptation in which zebrafish upregulate pigment production in response to constant darkness (36). Thus, the increase in basal levels of pigmentation could be connected to photoreceptor loss. In addition, pigment cells, called melanophores, can change skin color in response to environmental stimuli. This is mediated by release of the hormone epinephrine, which triggers intracellular changes in protein kinase A activity that result in increased dynein-mediated retrograde run lengths, leading to melanosome aggregation toward the melanophore cell body (16, 37, 38). Thus, to further test whether dynein activation is perturbed in *actr10*$^{nl15/nl15}$ mutant melanophores, we performed a classic melanosome aggregation assay (Fig. S2 *J*–*S*). In control animals, 5 min of exposure to epinephrine induced noticeable melanosome aggregation toward the center of the cell (Fig. S2*K*), whereas *actr10*$^{nl15/nl15}$ mutants maintained relatively dispersed melanosomes (Fig. S2*P*). After 30 min, whereas melanosomes in all control animals were aggregated (Fig. S2*N*), mutants continued to exhibit widespread pigment distribution (Fig. S2*S*), indicating

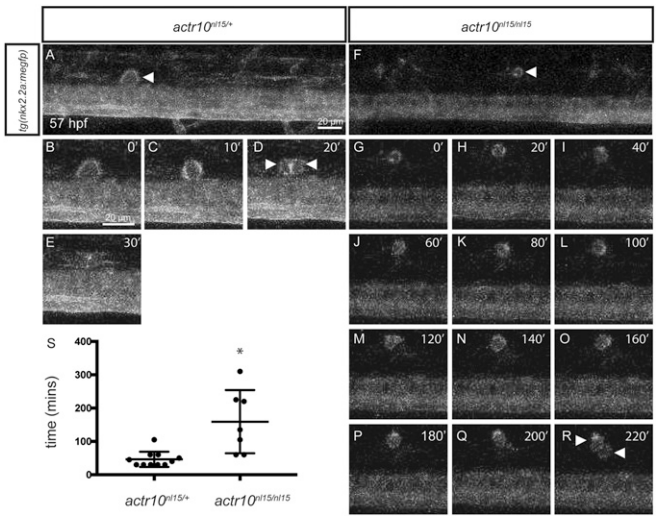

Fig. 4. Cell division is delayed in *actr10*$^{nl15/nl15}$ mutants. (*A*–*E*) Time-lapse imaging from ~57 hpf using the *tg(nkx2.2a:megfp)* line to mark OPCs allows for visualization of individual *nkx2.2a*-labeled cells that retract processes and become round in preparation for division (arrowhead, *A*). In *actr10*$^{nl15/+}$ heterozygous control animals, the cell remains in this state for only two panels of 10 min (*B* and *C*) before becoming two cells (arrowheads, *D*) that divide rapidly (*E*). (*F*–*R*) In contrast, a cell from an *actr10*$^{nl15/nl15}$ mutant animal that has already retracted its processes (arrowhead, *F*) takes over 3 h to divide (*G*–*R*). (*S*) Quantification revealed a significant difference in either time to cell division or the end of imaging between heterozygous control animals ($n = 11$ cells from five animals) and mutants ($n = 7$ cells from six animals; *$P < 0.02$, unpaired *t* test with Welch's correction). See also Movies S1–S4.

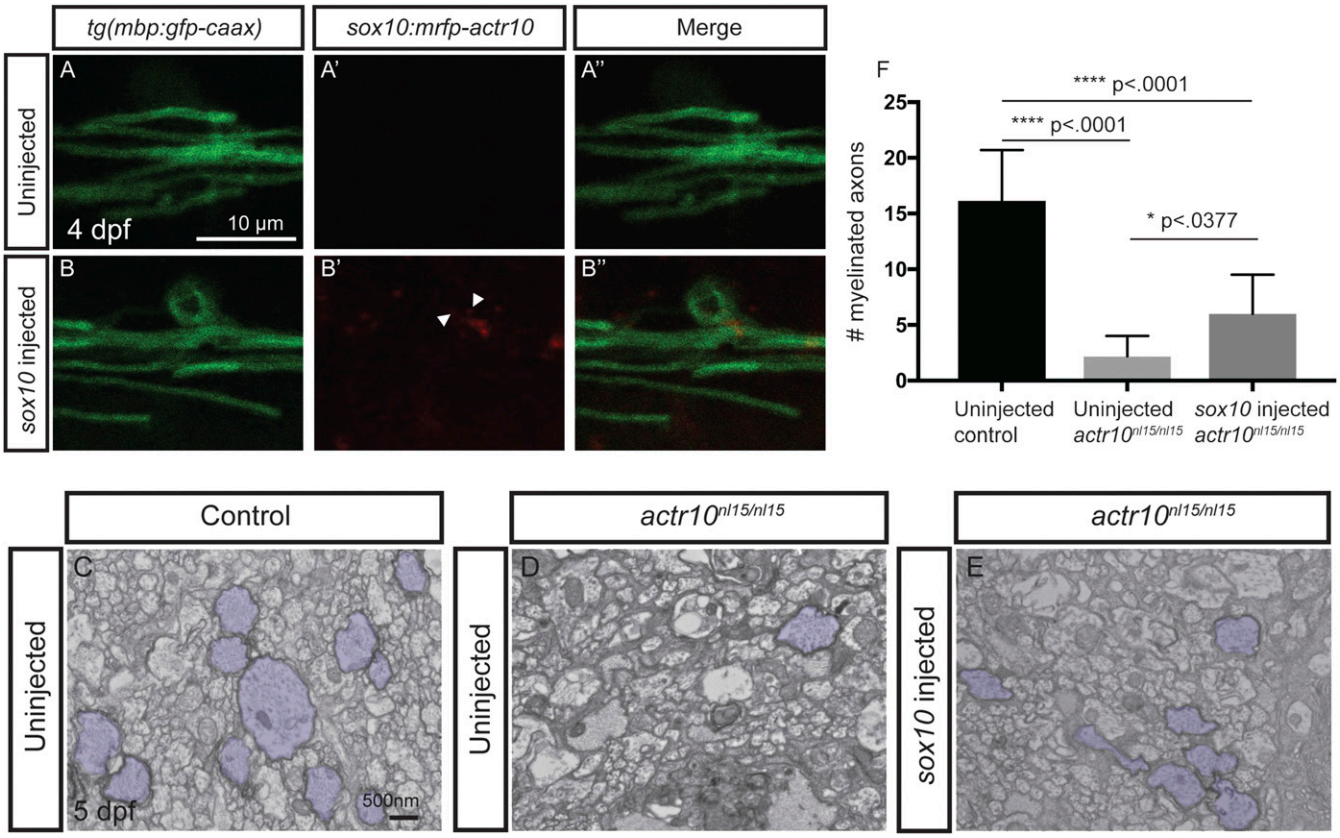

Fig. 5. Transient expression of *actr10* in oligodendrocytes partially suppresses myelination defects in *actr10*$^{nl15/nl15}$ mutants. (*A*–*B*′′) Confocal images of *mbp*-labeled oligodendrocytes in uninjected (*A*) and *sox10:mRFP-actr10* ("*sox10* injected") *actr10*$^{nl15/nl15}$ mutants (*B*). While uninjected *actr10*$^{nl15/nl15}$ mutants do not exhibit RFP fluorescence (*A*′ and *A*′′), injection of *sox10:mRFP-actr10* results in monomeric RFP fluorescence in *actr10*$^{nl15/nl15}$ mutants (*B*′ and *B*′′). (*C*–*E*) TEM images show dorsal spinal cords of uninjected WT and *actr10*$^{nl15/+}$ controls (*C*), uninjected *actr10*$^{nl15/nl15}$ mutants (*D*), and *sox10:mRFP-actr10*–injected *actr10*$^{nl15/nl15}$ mutants (*E*). Myelinated axons are pseudocolored in purple. (*F*) Quantification shows that *sox10*-injected *actr10*$^{nl15/nl15}$ mutants ($n = 6$) have significantly greater numbers of myelinated axons in the dorsal spinal cord compared with uninjected *actr10*$^{nl15/nl15}$ mutant siblings ($n = 5$, $P < 0.0377$), although *sox10:mRFP-actr10* injection does not restore myelination to WT control levels ($n = 5$, $P < 0.0001$), indicative of partial rescue. One-way ANOVA with Tukey's multiple comparisons test was used for statistical analyses.

that activated retrograde melanosome transport is compromised in mutant melanophores.

Actr10 Function in Oligodendrocytes Can Partially Suppress Myelin Defects. To understand the function of *actr10* in oligodendrocytes, a construct in which the glial *sox10* promoter drives expression of *actr10* tagged with monomeric RFP (*sox10:mRFP-actr10*) was transiently expressed in larvae from a cross between *tg(mbp:gfp-caax)*;*actr10*$^{nl15/+}$ and *actr10*$^{nl15/+}$ fish. *sox10:mRFP-actr10*–injected larvae (*sox10*-injected) exhibit RFP fluorescence, which is not seen in uninjected mutants (Fig. 5 *A*–*B*′′). TEM analysis and quantification at 5 dpf showed partial suppression of the mutant phenotype in the dorsal spinal cord (Fig. 5 *C*–*E*). Although *sox10:mRFP-actr10*–injected mutants were not rescued to control levels, *sox10:mRFP-actr10*–injected mutants possessed significantly more myelinated axons compared with uninjected mutant siblings, demonstrating that glial *actr10* rescue can promote proper myelination in vivo (Fig. 5*F*).

Analysis of a stable transgenic neuronal rescue line in which *mRFP-actr10* is driven by the neuronal-specific *neurod* promoter *tg(neurod:mRFP-actr10)* demonstrates that Actr10 also functions in neurons to promote oligodendrocyte myelination (Fig. S3). Given the critical functions of dynein/dynactin in all cells, it is not surprising that Actr10 functions in both neurons and oligodendrocytes to promote myelination. Of note, injection of *sox10:mRFP-actr10* resulted in lower levels of *actr10* as assayed by RFP fluorescence than were seen in the *tg(neurod:mRFP-actr10)* stable line. Thus, one reason a neuronal rescue was more effective could be due to the differences between transient injection with weak oligodendrocyte *actr10* expression and a stable transgenic line with strong *actr10* expression. The function of Actr10 in neurons to promote myelination forms the basis of future work; here, we focus on the cell-autonomous function of Actr10 in oligodendrocytes.

***actr10*$^{nl15/nl15}$ Mutants Have Reduced *mbp* mRNA Localization in Oligodendrocyte Processes.** All *actr10*$^{nl15/nl15}$ mutants observed have reduced *mbp* mRNA localization to processes at 4 dpf (Fig. 6 *A*–*F*). This phenotype cannot be explained by OPC proliferation defects alone, as the observation of dorsal elongating cells in mutants (Fig. 3) indicates that some oligodendrocytes are indeed migrating and maturing. Moreover, this phenotype is reminiscent of the kinesin *kif1b* zebrafish mutant in which disruption of anterograde transport results in accumulation of *mbp* mRNA in oligodendrocyte cell bodies (14). This led us to hypothesize that dynein/dynactin may play a role in efficient transport of *mbp* mRNA to distal oligodendrocyte processes.

Dynein and Dynactin Associate with *Mbp* mRNA Granules. To visualize *Mbp* mRNA transport, we expressed the MS2 reporter in primary rat oligodendrocyte cultures that were purified using the immunopanning technique and are free of neuronal contamination (39). MS2 is an RNA-binding protein derived from bacteriophage that binds with high affinity to specific RNA sequences that form stem loop structures (40). Using a bidirectional construct, we coexpressed

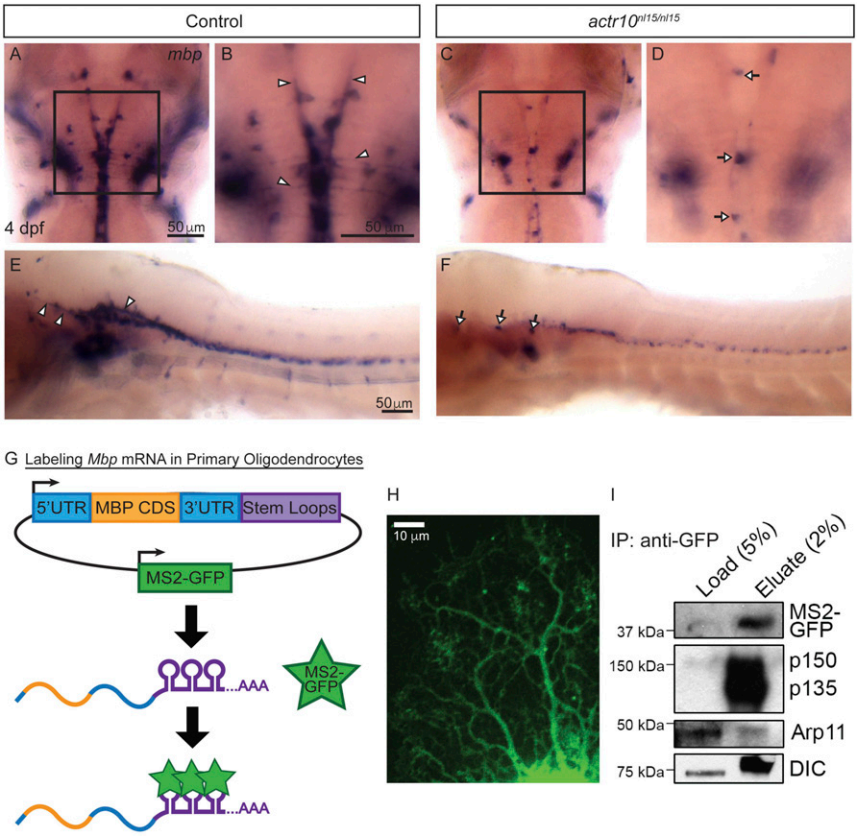

Fig. 6. Dynein and dynactin are associated with *Mbp* mRNA granules. (*A*) ISH shows robust levels of *mbp* mRNA in a representative control larva at 4 dpf, and higher magnification (*B*) shows *mbp* processes in the control (arrowheads) (n = 47/47). In contrast, an *actr10*$^{nl15/nl15}$ mutant (*C*) has a punctate *mbp* phenotype, and higher magnification of the same image (*D*) shows *mbp*-positive cell bodies (arrows) but no processes (n = 18/18). (*E*) A lateral view of the brain and spinal cord of a WT animal shows *mbp* mRNA in processes (arrowheads), while *actr10*$^{nl15/nl15}$ mutant animals (*F*) have cell bodies (arrows) but reduced *mbp* mRNA-bearing processes. (*G*) A bidirectional construct expressing MS2-GFP, a RNA-binding reporter, as well as MBP 5′UTR, CDS, and 3′UTR tagged with MS2 stem loops was electroporated into purified rat oligodendrocytes. MS2-GFP binds to stem loops to allow visualization of *Mbp* mRNA motility. (*H*) A primary rat oligodendrocyte expressing MS2-GFP–labeled *Mbp* mRNA imaged using spinning-disk confocal microscopy shows distribution of *Mbp* mRNA throughout the oligodendrocyte processes. (*I*) Lysates from primary rat oligodendrocytes expressing the MS2-GFP–labeled *Mbp* mRNA construct were immunoprecipitated using an anti-GFP antibody and probed with p150^{Glued}, DIC (dynein intermediate chain), and Actr10/Arp11 antibodies (n = 4 independent experiments).

two transcripts: (*i*) *Mbp* containing 5′UTR, CDS, and 3′UTR followed by MS2-binding stem loops and (*ii*) a GFP-tagged MS2 reporter (Fig. 6*G*). In oligodendrocytes differentiated in culture for 4 d, MS2-GFP–positive puncta associated with *Mbp* mRNA are distributed throughout the many processes that emanate outward from the cell body (Fig. 6*H*), while in control cells not expressing stem loops, MS2-GFP is retained in the cell body (Fig. S4*A*).

We can use this system to biochemically validate the association of the dynein motor and its adaptor dynactin to *Mbp* mRNA granules. Indeed, immunoprecipitations using a GFP antibody to isolate MS2-GFP–tagged *Mbp* mRNA granules also pulls out the dynactin subunit p150^{Glued}, dynein intermediate chain (DIC), and Arp11 (Fig. 6*I*). Eluates more robustly coimmunoprecipitated p150^{Glued} than DIC. Interestingly, two bands are visible using the p150^{Glued} antibody, which indicates that the lower band is p135, a shorter splice isoform of p150^{Glued} that does not contain the N-terminal microtubule-binding domain (41). This was confirmed by comparing the p135 band in this anti-GFP immunoprecipitation to another immunoprecipitation using an antibody against the N terminus of p150^{Glued} that preferentially isolates full-length p150^{Glued} but not p135 (Fig. S4 *B* and *C*). Thus, we have now demonstrated that the p135 isoform is expressed in oligodendrocytes and can associate with mRNA granules.

Acute Dynein Inhibition Arrests *Mbp* mRNA Transport in both Anterograde and Retrograde Directions. Live-cell imaging in this system using spinning-disk confocal microscopy reveals that processive *Mbp* mRNA transport occurs in both anterograde and retrograde directions with average speeds of ∼0.21 μm/s and 0.16 μm/s, respectively (Fig. 7 *A* and *B* and Movie S5), consistent with previously measured speeds for *Mbp* mRNA (4). To investigate the functional contribution of dynein in *Mbp* mRNA transport in oligodendrocytes, we pharmacologically inhibited dynein activity. The small-molecule cell-permeable dynein inhibitor ciliobrevin D works by disrupting the ATPase activity of the dynein motor and has a half-minimum inhibitory concentration (IC_{50}) ∼5–15 μM in the cilia (42). Cells acutely treated with 15 μM ciliobrevin were imaged for 60-s durations for up to an hour with no observed morphology changes or toxicity. As early as 4 min after ciliobrevin treatment, *Mbp* mRNA net speed decreases in both anterograde and retrograde directions (Fig. 7 *A* and *B*; n = 20 cells from two biological replicates). At around 10–15 min after ciliobrevin treatment, *Mbp* mRNA transport was arrested almost completely in both directions. When speeds are binned in 7-min increments, this decrease in speed is significantly different compared with untreated cells (Fig. 7 *C* and *D*).

Using faster frame rates to interrogate these possibilities, we saw as late as 11 min after ciliobrevin treatment *Mbp* mRNA that is engaged in bidirectional motility characterized by many frequent back-and-forth movements and directional switches (Fig. 7*A*, *Middle*). After ciliobrevin treatment, we also observe *Mbp* mRNA granules with zero net motility that are engaged in very rapid and frequent directional switches for durations of up to 1 min (Fig. S4*D*). This may represent a tug-of-war state during which anterograde and retrograde motor forces are roughly balanced and suggests that a single *Mbp* mRNA granule can associate simultaneously with both anterograde kinesin motors as well as retrograde dynein motors (Fig. 7*E*).

To confirm our findings in vivo, we treated WT zebrafish with ciliobrevin D for 21 h starting ∼3.5 dpf. Importantly, treating at this time point permits normal OPC development so that we can specifically examine the role of dynein in *mbp* mRNA transport. Although there was 15% mortality overall, importantly, the ciliobrevin-treated fish that were fixed at 4.5 dpf appeared grossly normal compared with vehicle-treated fish (Fig. S5 *A* and *B*). ISH for *mbp* mRNA revealed that ciliobrevin-treated fish had a significant reduction in *mbp* mRNA localized to oligodendrocyte processes compared with vehicle-treated controls (Fig. 7 *F*–*J*).

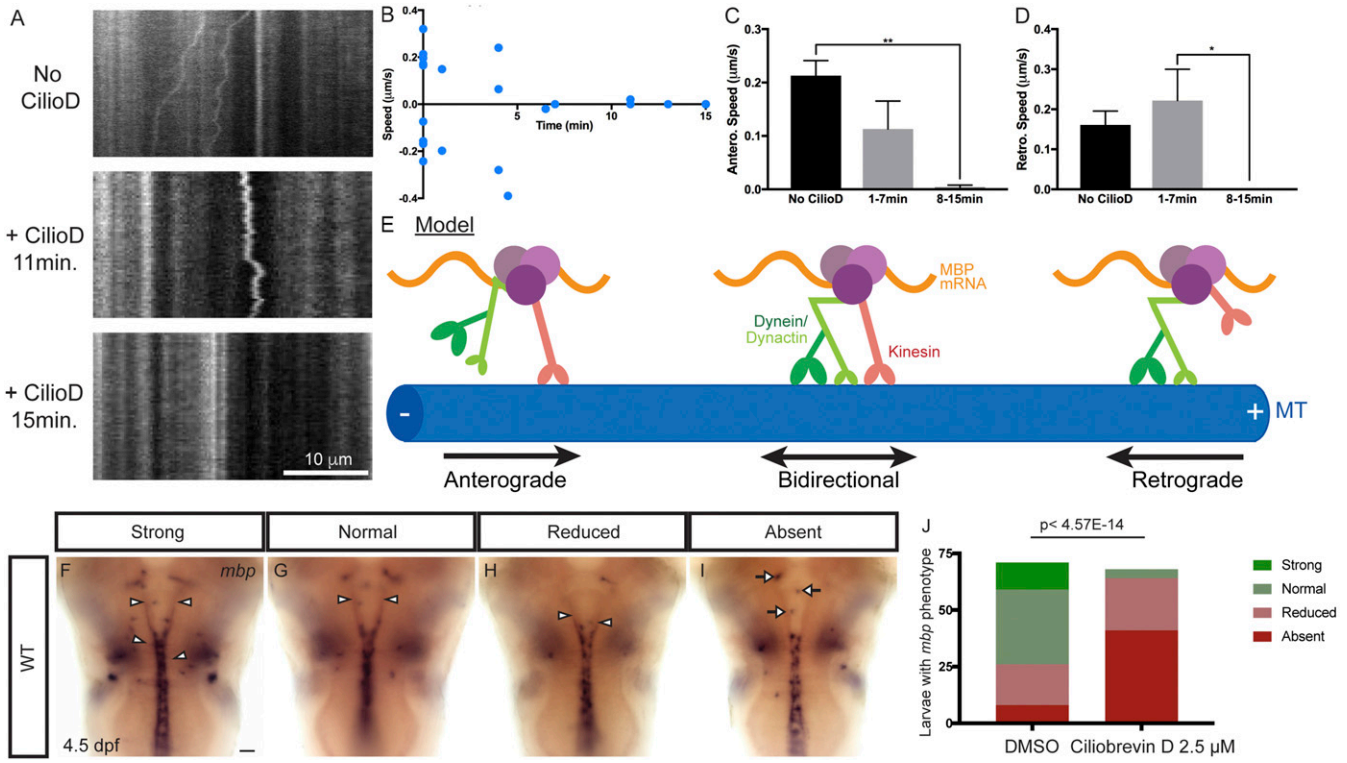

Fig. 7. Acute dynein inhibition arrests both anterograde and retrograde *Mbp* mRNA transport in cultured oligodendrocytes and perturbs *mbp* localization in zebrafish. (*A*) In kymographs representing 60 s of live-cell imaging, MS2-GFP–labeled *Mbp* mRNA can be seen moving in the retrograde direction in untreated cells (*Top*). Following acute ciliobrevin D (15 μM) addition, *Mbp* mRNA displays bidirectional motility characterized by frequent back-and-forth movement and many directional switches (*Middle*). Finally, around 15 min after ciliobrevin D (15 μM) addition, most cells display arrested motility (*Bottom*). (*B*) A scatter plot represents the average anterograde or retrograde net speeds for individual oligodendrocytes. (*C* and *D*) Anterograde or retrograde net speeds were averaged for each cell and binned across 27-min time periods following ciliobrevin treatment. At 8–15 min following ciliobrevin treatment, speeds significantly decreased compared with earlier time points. One-way ANOVAs with post hoc Tukey's test were performed. Anterograde speeds: No CilioD vs. 1–7 min, $P = 0.11$; No CilioD vs. 8–15 min, $^{**}P = 0.0011$; 1–7 min vs. 8–15 min, $P = 0.077$. Retrograde speeds: No CilioD vs. 1–7 min, $P = 0.67$; No CilioD vs. 8–15 min, $P = 0.11$, 1–7 min vs. 8–15 min, $^{*}P = 0.027$. (*E*) A model shows that *Mbp* mRNA granules can move processively in the anterograde and retrograde directions as well as bidirectionally and that each *Mbp* mRNA granule can simultaneously bind to both kinesin and the dynein/dynactin complex. (*F–I*) *mbp* ISH of zebrafish larvae treated with ciliobrevin D for 21 h. Larvae were scored as having strong (*F*), normal (*G*), reduced (*H*), or absent (*I*) *mbp* localization in oligodendrocyte processes (arrowheads, processes; arrows, cell bodies). (*J*) Quantification of phenotypic distribution shows that there was a significant difference in scores for DMSO ($n = 71$) and ciliobrevin D-treated larvae ($n = 68$), with the latter exhibiting more larvae with reduced or absent *mbp* localization in oligodendrocyte processes ($P < 4.5E\text{-}14$, Fisher's exact test). (Scale bar, 50 μM.)

Taken together, our in vitro and in vivo results show that dynein inhibition leads to reduced *mbp* mRNA distribution.

Chronic Dynein Inhibition Disrupts MBP Protein Translation in Cultured Oligodendrocytes and Disrupts Myelination in Zebrafish. To understand how *Mbp* mRNA transport inhibition can lead to myelination defects, we asked whether *Mbp* mRNA transport is necessary for local MBP protein translation. We hypothesized that proper translocation of *Mbp* mRNA granules precedes local translation and recruitment of ribosomes (Fig. 8*A*). To test this, we treated cultured rat oligodendrocytes for 21 h with the dynein inhibitor ciliobrevin, then visualized *Mbp* mRNA localization using single molecule FISH (fluorescent ISH) and simultaneously immunostained for MBP protein. Previously, oligodendrocytes were treated acutely with 15 μM ciliobrevin for less than 1 h for live-cell imaging. However, chronic treatment for 21 h at this concentration resulted in some toxicity compared with control and vehicle-treated conditions (Fig. S5*C*). Thus, cells that had been differentiated for 3 d in vitro were treated for 21 h at the nontoxic concentration of 5 μM ciliobrevin (Fig. S5*C*), which had been previously used for overnight dynein inhibition in neurons (43).

Ciliobrevin-treated cells had remarkably decreased *Mbp* mRNA distribution and less MBP protein (Fig. 8 *B* and *C*). Whereas *Mbp* mRNA granules in control cells were dispersed throughout the oligodendrocyte processes as distally as the cell periphery, *Mbp* mRNA granules in ciliobrevin-treated cells were restricted to the cell body and to proximal processes. Consistent with live-cell imaging results from acute ciliobrevin treatment, this chronic 21-h treatment also demonstrates that dynein inhibition disrupts distal *Mbp* mRNA localization. Quantification of MBP protein staining revealed that only 42% of ciliobrevin-treated cells contained MBP protein, compared with 63% and 62% of control and vehicle-treated cells, respectively. These MBP-containing cells can be further binned as low expressers that have punctate MBP protein localization and high expressers that display pancake-like widespread MBP protein distribution. Binning demonstrates that while 29% and 27% of control and vehicle-treated cells are high expressers, only 8.5% of ciliobrevin-treated cells are high expressers. These data indicate that dynein inhibition leads to inefficient MBP translation.

Discussion

Myelination by oligodendrocytes is critical for proper function of the nervous system. In a forward genetic screen in zebrafish, we identified the dynactin subunit Actr10 as a regulator of myelination. *actr10* mutants are lethal and display signs of impeded dynein loss of function in some tissues, including blindness due to photoreceptor loss and aberrant pigment cells with defects in melanosome motility. In the nervous system, mutants have fewer myelinated axons by TEM and fewer OPCs in part due to proliferation defects, phenocopying a previously described dynein

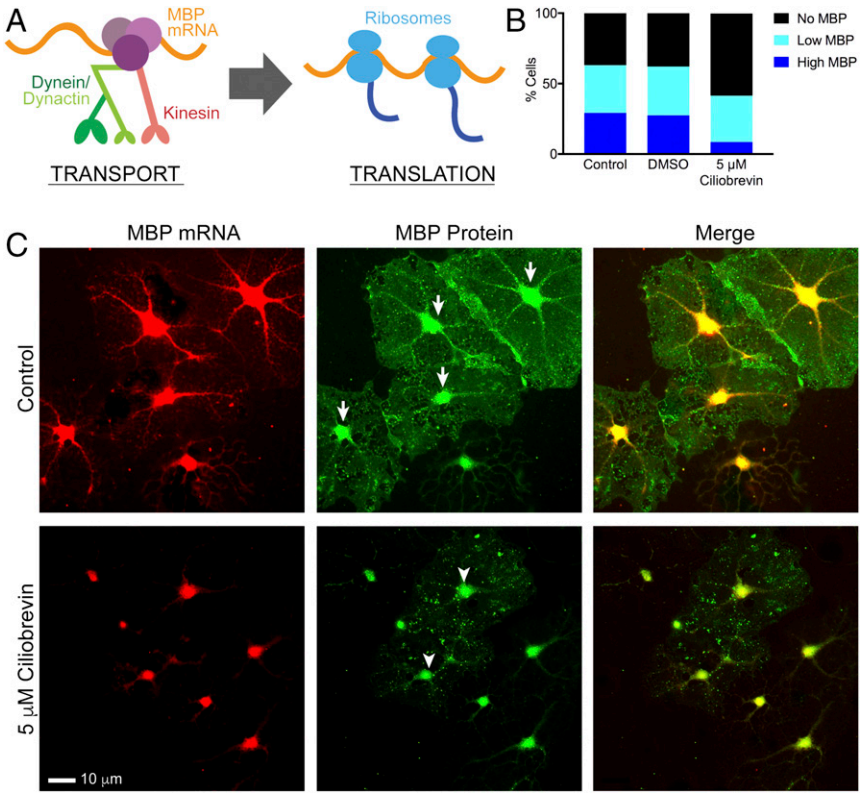

Fig. 8. Chronic dynein inhibition disrupts MBP protein translation in cultured oligodendrocytes and disrupts myelination in zebrafish. (*A*) A model shows that transport of *Mbp* mRNA granules by microtubule-based motors precedes local translation and recruitment of ribosomes. (*B*) Quantification of the percentage of DIV3 oligodendrocytes treated for 21 h with 5 μM ciliobrevin that express MBP protein demonstrate that a lower percentage of ciliobrevin-treated cells (42%) are positive for MBP protein compared with control cells (63%, $P < 0.001$) and DMSO-treated cells (62%, $P < 0.001$). Of these MBP-containing cells, only 8.5% of ciliobrevin-treated cells highly expressed MBP protein compared with 29% ($P < 0.001$) and 27% ($P < 0.001$) in control and DMSO-treated cells. (*C*) Cells treated with 5 μM ciliobrevin for 21 h were costained with single-molecule FISH probes against *Mbp* mRNA and with a monoclonal antibody against MBP protein. MBP protein images (*Middle*) show examples of high expressers (arrows) in control cells and low expressers (arrowheads) in ciliobrevin-treated cells ($n = 2$ biological replicates using primary cultures from two different animals, four coverslips, 23–32 fields of view per group).

zebrafish mutant (16). In addition, mutants exhibit less *mbp* mRNA in oligodendrocyte processes, similar to previous observations made in kinesin *kif1b* zebrafish mutants (14). Thus, we propose that proper function of the retrograde motor dynein and its adaptor dynactin is paradoxically required for anterograde transport of *mbp* mRNA. Indeed, we demonstrate in purified rodent oligodendrocyte cultures that acute pharmacological inhibition of dynein activity arrests *Mbp* mRNA transport in both anterograde and retrograde directions. Moreover, ciliobrevin treatment also decreases MBP protein levels, suggesting that mRNA transport is necessary for local translation of MBP. We confirmed these results in vivo in ciliobrevin-treated zebrafish, in which *mbp* mRNA distribution is perturbed in oligodendrocytes.

The combination of our in vivo and cellular data suggests that dynein/dynactin activity is necessary for anterograde *Mbp* mRNA transport. In zebrafish, both Actr10/Arp11 loss of function and chronic dynein inhibition prevent proper anterograde distribution of *mbp* mRNA in oligodendrocytes. In cultured oligodendrocytes, acute dynein inhibition disrupts *Mbp* mRNA transport in both anterograde and retrograde directions. Our transport results are consistent with ciliobrevin treatment of cultured dorsal root ganglion neurons, which display arrest of mitochondrial and lysosomal axonal transport in both anterograde and retrograde directions (43, 44). Furthermore, our observations are consistent with earlier experiments in *Drosophila* macrophage-like S2 cells that demonstrate dynein knockdown leads to arrested transport in both anterograde and retrograde directions of fluorescently tagged RNA-binding protein FMRP (22).

Our results also demonstrate that mRNA granules are highly heterogeneous, both in motility and in composition. We observe *Mbp* mRNA granules that move quickly with average net speeds ~0.21 and 0.16 μm/s in anterograde and retrograde directions, respectively; we also observe *Mbp* mRNA granules that have very little net motility and move bidirectionally with frequent directional switches. Each bidirectional mRNA granule likely associates with multiple opposing motors that are engaged in a "tug of war" in which opposing motor forces are nearly balanced. Since one kinesin has 7 pN of unitary force while one dynein only has 1 pN of unitary force, this suggests that a bidirectional mRNA granule likely associates with at least 1 kinesin and 6–8 dyneins. Thus, our data support a model whereby each *Mbp* mRNA granule simultaneously associates with kinesin and dynein/dynactin and the full assembly of opposing motors may be required to sustain transport (Fig. 7*E*). Though it is unclear why both kinesins and dyneins are simultaneously associated with individual cargos, one possibility is that the ability to transiently step back and forth may allow more flexibility in circumnavigating roadblocks or switching microtubules (45). This may be particularly important in the crowded cytoskeletal environment of the oligodendrocyte, in which microtubules penetrate many concentric layers of the dense myelin sheath (46).

Moreover, association of different dynactin isoforms with mRNA granules may play a role in regulating *Mbp* mRNA transport as well. Coimmunoprecipitations revealed that *Mbp* mRNA granules associate with not only $p150^{Glued}$ but also its shorter isoform p135, which is unable to bind to microtubules (41). Though a human neuronal cell line was used for the original characterization of p135, we now show that p135 is also present in primary oligodendrocytes. Though it is still unclear what functional role p135 may play in transport regulation, a classic in vivo labeling study in the optic nerve demonstrated that $p150^{Glued}$-associated cargos traveled much faster than p135-associated cargos, arriving past the optic chiasm at 2 d and 4 d after initial labeling, respectively (47).

These data highlight that there is much more to learn about the composition of vertebrate mRNA granules, including how many motors are associated and what adaptor proteins link these motors to mRNAs. In neuronal axons, the RNA-binding protein La is transported in the anterograde direction in its native form and in the retrograde direction in its sumoylated form; sumoylation is required for dynein association to La and may act as a mechanism to return mRNA-free La protein to the nucleus by decreasing its ability to bind to mRNA (48). Furthermore, transport of mRNA in neurons can be stimulated in response to neuronal activity (49, 50),

and in oligodendrocytes, activation of Fyn kinase has been shown to trigger MBP translation (6–8). Further research on regulation at the adaptor level may yield clues on how environmental stimuli can trigger *Mbp* mRNA transport in oligodendrocytes.

Together, our results suggest that *actr10* mutants display phenotypes similar to dynein/dynactin loss of function in photoreceptors, melanophores, and oligodendrocytes. Interestingly, recently identified human patients with mutations in dynein and dynactin primarily present with sensory and motor neuron symptoms and are diagnosed with Charcot–Marie–Tooth distal neuropathy or spinal muscular atrophy (51–60). Thus, in both humans and zebrafish, the nervous system is exquisitely sensitive to mutations in dynein and dynactin. Though a link between myelination and dynein/dynactin mutations has not been established in humans, our work in zebrafish and mammalian oligodendrocytes demonstrates that dynein/dynactin function in *Mbp* mRNA transport is critical for proper myelination in vivo.

Materials and Methods

Zebrafish Lines and Rearing Conditions. All zebrafish work was approved by the Washington University IRB and was performed in compliance with Washington University institutional animal protocols (animal protocol no. 20160174; Institutional Biological & Chemical (IBC) Safety Committee protocol no. 10-643), and zebrafish were housed in the Washington University zebrafish facility (zebrafish.wustl.edu). Embryos were raised in incubators at 28.5 °C in egg water (5 mM NaCl, 0.17 mM KCl, 0.33 mM $CaCl_2$, 0.33 mM $MgSO_4$). ENU mutagenesis was performed according to standard protocols (61), and larvae were screened at 5 dpf for myelin abnormalities by two transgenes, *tg(lhx1a:gfp)* and *tg(mbp:mCherry)*, as well as by ISH for *mbp* mRNA levels. The following transgenic and mutant zebrafish lines were used: SAT, SJD (62), $actr10^{stl83}$, $actr10^{nl15}$ (25), *tg(lhx1a:gfp)* (23), *tg(mbp:mCherry)* (a kind gift from Dave Lyons, University of Edinburgh, Edinburgh), *tg(neurod:egfp)* (63), *tg(olig2:dsred)* (26), *tg(sox10:mgfp)* (27), *tg(nkx2.2a:megpf)* (1), and *tg(mbp:gfp-caax)* (64).

Whole Genome Sequencing and Mapping. The F2 generation of *stl83* heterozygotes was outcrossed to SJD and raised. These animals were intercrossed, and F4 progeny were screened for axonal swellings. DNA was extracted from phenotypically WT and mutant larvae at 5 dpf and sent to the Genome Technology Access Center (GTAC) at Washington University for whole genome sequencing. An in-house analysis pipeline (24) was used to determine that the mutant-to-WT allele ratio was highest on chromosome 20. A SNP subtraction analysis using other whole genome sequencing datasets narrowed the number of possible mutations down to five. The gene was confirmed by a complementation test using the $actr10^{nl15}$ allele (25).

Genotyping. A derived cleaved amplified polymorphic sequences (dCAPS) assay was developed to genotype the $actr10^{stl83}$ allele (helix.wustl.edu/dcaps/dcaps.html). An A-to-C mismatch is introduced in the forward primer (forward primer: 5′-GTCAGAGAACTTGCTGATACTC-3′; reverse primer: 5′-AGCAGTTCAGGGCAGCTTTA-3′). This causes an AvaI restriction digest site in the WT haplotype, and digestion generates two visible WT products of 22 and 224 bp and a mutant product of 244 bp. To genotype the $actr10^{nl15}$ allele, PCR was used to amplify the first exon (forward primer: 5′-ACCCAGCCGTTCCTCTAATG-3′; reverse primer: 5′-CCGCTCCTAAATCAATCACC-3′). Mutagenesis introduced a T-to-G mutation in the start site. This inserts an HaeIII site, and digestion results in two WT fragments of 126 and 50 bp and three mutant fragments of 112, 50, and 14 bp.

ISH. In brief, embryos were treated with 0.003% phenylthiourea (PTU) at 24 hpf to prevent pigmentation. Embryos were reared in egg water with PTU until the desired age and fixed in 4% paraformaldehyde overnight at 4 °C in 1.5 mL Eppendorf tubes with ∼20 embryos per tube. A standard ISH protocol was then used (65), and all phenotypes were scored blindly.

TEM. TEM was done according to standard protocols (66). More detail can be found in *SI Materials and Methods*.

Marker Analysis Using Transgenes. Two transgenes, *tg(olig2:dsred)* and *tg(sox10:mgfp)*, were crossed into an $actr10^{nl15/+}$ background and grown to adulthood. Animals were intercrossed to produce double transgene labeling, screened for double fluorescence, and fixed at 3 dpf for OPC cross-section analysis. Single transgene *tg(olig2:dsred)* animals were used to count the number of dorsal, elongated *olig2*-labeled cells at 3 and 4 dpf. For details, see *SI Materials and Methods*.

Time-Lapse Imaging. *tg(nkx2.2a:megfp)*;$actr10^{nl15/+}$ and $actr10^{nl15/+}$ animals were crossed, and live imaging was performed for up to 12 h beginning at 57 hpf on a Zeiss LSM 880 confocal microscope. For details, see *SI Materials and Methods*.

Melanosome Aggregation. Control and $actr10^{nl15/nl15}$ mutants were separated at 3 dpf by pigment phenotype. Larvae were treated with 0.5 mg/mL epinephrine (Sigma-Aldrich) dissolved in egg water. One representative animal from control and mutant groups was selected at random, treated with tricaine, mounted on an agarose mold, imaged, and returned to the epinephrine treatment. This was repeated approximately every 5 min, from 5 to 15 min, and again at 30 min. After 30 min, larvae were collected and genotyped.

Noldus DanioVision Assay. The Noldus DanioVision system was used to determine whether mutants were blind. Larvae were placed individually in a 96-well plate, and the following protocol was used: light on (baseline) 0–4 min, light off (dark response) 4–8 min, light on (recovery) 8–12 min. The average distance moved from the center point during the baseline, and dark response was calculated and analyzed for statistical significance. Two technical replicates were performed.

Primary Rat Oligodendrocyte Culture and Electroporation. All rodent work was approved by the Stanford University IRB and was performed in compliance with Stanford University institutional animal protocols (animal protocol no. 10726). OPCs were purified from enzymatically dissociated P6–P8 Sprague–Dawley (Charles River) rat brain cortices by immunopanning and differentiated in serum-free defined medium containing T3, as previously described (39). Cells were electroporated using Amaxa Nucleofector (Program O-17 for rat oligodendrocytes; Lonza) with a bicistronic construct (pBI; Clontech) simultaneously expressing MBP 5′UTR, CDS, 3′UTR, and MS2-binding stem loops (24x) as well as MS2-GFP (40, 67).

Live-Cell Imaging and Ciliobrevin D Treatment. Live-cell imaging was performed at the Stanford Cell Sciences Imaging Facility on a Nikon spinning disk confocal (TiE inverted microscope body equipped with Perfect Focus mechanism, Yokogawa spinning disk) with an Andor EMCCD camera inside an environmental chamber (37 °C, CO_2). Cells were treated with 15 μM ciliobrevin D (Calbiochem), and images were acquired at 1–3 frames per second for 60 s for a different cell at each time point to minimize photobleaching. Kymographs were generated from these movies using the Multiple Kymographs plug-in (FIJI, NIH) with a line width of 3 pixels. Net speed was calculated from the net duration and net distance of each motile event and represented as the average net speed for each cell. $n = 2$ biological replicates (two OPC preps from two different animals), 10 imaging plates, 20 cells. WT zebrafish at 3.5 dpf were separated into six-well plates with 20 larvae per well. Larvae were treated with either 2.5 μM ciliobrevin D (Calbiochem) or DMSO vehicle in egg water for 21 h. Larvae were fixed in 4% paraformaldehyde for ISH after 21 h and scored blindly for localization of *mbp* mRNA in oligodendrocyte processes.

Coimmunoprecipitations. We lysed 1–4 million primary oligodendrocytes per condition in HEM buffer (50 mM Hepes, 1 mM EDTA, 1 mM $MgCl_2$) containing 25 mM NaCl, 0.5% Triton X-100, and protease inhibitors (P8340; Sigma). Cell lysates were incubated with Protein-G Dynabeads (Invitrogen), and coimmunoprecipitations were performed following the manufacturer's instructions using a monoclonal antibody against GFP (JL-8; Clontech). Western blots were probed with antibodies against DIC (Chemicon), $p150^{Glued}$ (610474; BD Transduction), and Actr10 (rabbit polyclonal, 20101–1-AP; Proteintech).

Single-Molecule FISH. Single-molecule FISH probes were designed against *Mbp* mRNA CDS (Stellaris; LGC Biosearch Technologies). Cells were stained according to the manufacturer's protocol. Briefly, cells were fixed in 4% paraformaldehyde, permeabilized in 70% ethanol for 1 h at 4 °C, hybridized with single-molecule FISH probes and primary antibody against MBP (ab7349; Abcam) for 4–16 h at 37 °C, washed for 30 min at 37 °C, and then stained with secondary antibody.

Statistical Analysis. GraphPad Prism 7 and RStudio were used for statistical analysis. Unpaired *t* tests with Welch's correction were used for comparing all experiments with two variables. A one-way ANOVA was used to calculate the glial and neuronal TEM rescue experiments. Fisher's exact test in R was used for calculating the ciliobrevin D experiments in zebrafish.

ACKNOWLEDGMENTS. We thank members of the Solnica-Krezel laboratory, C. Johnson, Z. Spence, and S. Canter for assistance with the screen and fish maintenance; members of the K.R.M. laboratory and Matt McCoy for helpful discussions; D. Lyons for transgenic fish lines; and P. Gontarz for assistance with statistical analyses. A.L.H. is supported by the Philip and Sima Needleman Student Fellowship in Regenerative Medicine (St. Louis) and by National Institute of Neurological Disorders and Stroke (NINDS) Grant F31 NS096814, and M.-m.F. is supported by National Institute of Child Health and Human Development (NICHD) Grant T32 HD7249 and NINDS Grant F32 NS090721 and a National Multiple Sclerosis Society (NMSS) postdoctoral fellowship. This work was also supported by NINDS Grants F31 NS094004 (to B.L.H.), F31 NS087801 (to S.D.A.), and National Institute of General Medical Sciences (NIGMS) Grant R01 GM056988 (to S.L.J.); the Dr. Miriam and Sheldon G. Adelson Medical Research Foundation (Las Vegas) (B.A.B.); a Myra Reinhard Foundation grant (Los Gatos, CA) (to B.A.B.); and NICHD Grant R01 HD80601 (to K.R.M.). K.R.M. is a Harry Weaver Neuroscience Scholar of the NMSS.

1. Kirby BB, et al. (2006) In vivo time-lapse imaging shows dynamic oligodendrocyte progenitor behavior during zebrafish development. *Nat Neurosci* 9:1506–1511.
2. Simons M, Nave KA (2015) Oligodendrocytes: Myelination and axonal support. *Cold Spring Harb Perspect Biol* 8:a020479.
3. Aggarwal S, et al. (2013) Myelin membrane assembly is driven by a phase transition of myelin basic proteins into a cohesive protein meshwork. *PLoS Biol* 11:e1001577.
4. Ainger K, et al. (1993) Transport and localization of exogenous myelin basic protein mRNA microinjected into oligodendrocytes. *J Cell Biol* 123:431–441.
5. Colman DR, Kreibich G, Frey AB, Sabatini DD (1982) Synthesis and incorporation of myelin polypeptides into CNS myelin. *J Cell Biol* 95:598–608.
6. Czopka T, Ffrench-Constant C, Lyons DA (2013) Individual oligodendrocytes have only a few hours in which to generate new myelin sheaths in vivo. *Dev Cell* 25:599–609.
7. Wake H, Lee PR, Fields RD (2011) Control of local protein synthesis and initial events in myelination by action potentials. *Science* 333:1647–1651.
8. White R, et al. (2008) Activation of oligodendroglial Fyn kinase enhances translation of mRNAs transported in hnRNP A2-dependent RNA granules. *J Cell Biol* 181:579–586.
9. Nawaz S, et al. (2015) Actin filament turnover drives leading edge growth during myelin sheath formation in the central nervous system. *Dev Cell* 34:139–151.
10. Zuchero JB, et al. (2015) CNS myelin wrapping is driven by actin disassembly. *Dev Cell* 34:152–167, and correction (2015) 34:608.
11. Carson JH, Worboys K, Ainger K, Barbarese E (1997) Translocation of myelin basic protein mRNA in oligodendrocytes requires microtubules and kinesin. *Cell Motil Cytoskeleton* 38:318–328.
12. Lunn KF, Baas PW, Duncan ID (1997) Microtubule organization and stability in the oligodendrocyte. *J Neurosci* 17:4921–4932.
13. Kardon JR, Vale RD (2009) Regulators of the cytoplasmic dynein motor. *Nat Rev Mol Cell Biol* 10:854–865.
14. Lyons DA, Naylor SG, Scholze A, Talbot WS (2009) Kif1b is essential for mRNA localization in oligodendrocytes and development of myelinated axons. *Nat Genet* 41:854–858.
15. Langworthy MM, Appel B (2012) Schwann cell myelination requires Dynein function. *Neural Dev* 7:37.
16. Yang ML, et al. (2015) CNS myelination requires cytoplasmic dynein function. *Dev Dyn* 244:134–145.
17. Hancock WO (2014) Bidirectional cargo transport: Moving beyond tug of war. *Nat Rev Mol Cell Biol* 15:615–628.
18. Waterman-Storer CM, et al. (1997) The interaction between cytoplasmic dynein and dynactin is required for fast axonal transport. *Proc Natl Acad Sci USA* 94:12180–12185.
19. Martin M, et al. (1999) Cytoplasmic dynein, the dynactin complex, and kinesin are interdependent and essential for fast axonal transport. *Mol Biol Cell* 10:3717–3728.
20. Encalada SE, Szpankowski L, Xia CH, Goldstein LSB (2011) Stable kinesin and dynein assemblies drive the axonal transport of mammalian prion protein vesicles. *Cell* 144:551–565.
21. Moughamian AJ, Holzbaur ELF (2012) Dynactin is required for transport initiation from the distal axon. *Neuron* 74:331–343.
22. Ling S-C, Fahrner PS, Greenough WT, Gelfand VI (2004) Transport of Drosophila fragile X mental retardation protein-containing ribonucleoprotein granules by kinesin-1 and cytoplasmic dynein. *Proc Natl Acad Sci USA* 101:17428–17433.
23. Swanhart LM, et al. (2010) Characterization of an lhx1a transgenic reporter in zebrafish. *Int J Dev Biol* 54:731–736.
24. Sanchez NE, et al. (2017) Whole genome sequencing-based mapping and candidate identification of mutations from fixed zebrafish tissue. *G3*, 10.1534/g3.117.300212.
25. Drerup CM, Herbert AL, Monk KR, Nechiporuk AV (2017) Regulation of mitochondria-dynactin interaction and mitochondrial retrograde transport in axons. *Elife* 6:1–25.
26. Shin J, Park HC, Topczewska JM, Mawdsley DJ, Appel B (2003) Neural cell fate analysis in zebrafish using olig2 BAC transgenics. *Methods Cell Sci* 25:7–14.
27. Ackerman SD, Garcia C, Piao X, Gutmann DH, Monk KR (2015) The adhesion GPCR Gpr56 regulates oligodendrocyte development via interactions with Gα12/13 and RhoA. *Nat Commun* 6:6122.
28. Mathews ES, Appel B (2016) Oligodendrocyte differentiation. *Methods Cell Biol* 134: 69–96.
29. Yeh T-Y, Quintyne NJ, Scipioni BR, Eckley DM, Schroer TA (2012) Dynactin's pointed-end complex is a cargo-targeting module. *Mol Biol Cell* 23:3827–3837.
30. Zhang J, et al. (2008) Arp11 affects dynein-dynactin interaction and is essential for dynein function in Aspergillus nidulans. *Traffic* 9:1073–1087.
31. Del Bene F, Wehman AM, Link BA, Baier H (2008) Regulation of neurogenesis by interkinetic nuclear migration through an apical-basal notch gradient. *Cell* 134:1055–1065.
32. Tsujikawa M, Omori Y, Biyanwila J, Malicki J (2007) Mechanism of positioning the cell nucleus in vertebrate photoreceptors. *Proc Natl Acad Sci USA* 104:14819–14824.
33. Jing X, Malicki J (2009) Zebrafish ale oko, an essential determinant of sensory neuron survival and the polarity of retinal radial glia, encodes the p50 subunit of dynactin. *Development* 136:2955–2964.
34. MacPhail RC, et al. (2009) Locomotion in larval zebrafish: Influence of time of day, lighting and ethanol. *Neurotoxicology* 30:52–58.
35. Serra EL, Medalha CC, Mattioli R (1999) Natural preference of zebrafish (Danio rerio) for a dark environment. *Braz J Med Biol Res* 32:1551–1553.
36. Neuhauss SC, et al. (1999) Genetic disorders of vision revealed by a behavioral screen of 400 essential loci in zebrafish. *J Neurosci* 19:8603–8615.
37. Clark TG, Rosenbaum JL (1982) Pigment particle translocation in detergent-permeabilized melanophores of Fundulus heteroclitus. *Proc Natl Acad Sci USA* 79:4655–4659.
38. Tuma MC, Gelfand VI (1999) Molecular mechanisms of pigment transport in melanophores. *Pigment Cell Res* 12:283–294.
39. Dugas JC, Emery B (2013) Purification of oligodendrocyte precursor cells from rat cortices by immunopanning. *Cold Spring Harb Protoc* 2013:745–758.
40. Bertrand E, et al. (1998) Localization of ASH1 mRNA particles in living yeast. *Mol Cell* 2:437–445.
41. Tokito MK, Howland DS, Lee VM, Holzbaur EL (1996) Functionally distinct isoforms of dynactin are expressed in human neurons. *Mol Biol Cell* 7:1167–1180.
42. Firestone AJ, et al. (2012) Small-molecule inhibitors of the AAA+ ATPase motor cytoplasmic dynein. *Nature* 484:125–129.
43. Sainath R, Gallo G (2015) The dynein inhibitor Ciliobrevin D inhibits the bidirectional transport of organelles along sensory axons and impairs NGF-mediated regulation of growth cones and axon branches. *Dev Neurobiol* 75:757–777.
44. Roossien DH, Lamoureux P, Miller KE (2014) Cytoplasmic dynein pushes the cytoskeletal meshwork forward during axonal elongation. *J Cell Sci* 127:3593–3602.
45. Fu MM, Holzbaur EL (2014) Integrated regulation of motor-driven organelle transport by scaffolding proteins. *Trends Cell Biol* 24:564–574.
46. Snaidero N, et al. (2014) Myelin membrane wrapping of CNS axons by PI(3,4,5)P3-dependent polarized growth at the inner tongue. *Cell* 156:277–290.
47. Dillman JF, 3rd, Dabney LP, Pfister KK (1996) Cytoplasmic dynein is associated with slow axonal transport. *Proc Natl Acad Sci USA* 93:141–144.
48. van Niekerk EA, et al. (2007) Sumoylation in axons triggers retrograde transport of the RNA-binding protein La. *Proc Natl Acad Sci USA* 104:12913–12918.
49. Buxbaum AR, Wu B, Singer RH (2014) Single β-actin mRNA detection in neurons reveals a mechanism for regulating its translatability. *Science* 343:419–422.
50. Park HY, et al. (2014) Visualization of dynamics of single endogenous mRNA labeled in live mouse. *Science* 343:422–424.
51. Braathen GJ, et al. (2016) Variants in the genes DCTN2, DNAH10, LRIG3, and MYO1A are associated with intermediate Charcot-Marie-Tooth disease in a Norwegian family. *Acta Neurol Scand* 134:67–75.
52. Weedon MN, et al. (2011) Exome sequencing identifies a DYNC1H1 mutation in a large pedigree with dominant axonal Charcot-Marie-Tooth disease. *Am J Hum Genet* 89:308–312.
53. Fiorillo C, et al. (2014) Novel dynein DYNC1H1 neck and motor domain mutations link distal spinal muscular atrophy and abnormal cortical development. *Hum Mutat* 35:298–302.
54. Harms MB, et al. (2012) Mutations in the tail domain of DYNC1H1 cause dominant spinal muscular atrophy. *Neurology* 78:1714–1720.
55. Niu Q, Wang X, Shi M, Jin Q (2015) A novel DYNC1H1 mutation causing spinal muscular atrophy with lower extremity predominance. *Neurol Genet* 1:e20.
56. Peeters K, et al. (2015) Novel mutations in the DYNC1H1 tail domain refine the genetic and clinical spectrum of dyneinopathies. *Hum Mutat* 36:287–291.
57. Punetha J, et al. (2015) Exome sequencing identifies DYNC1H1 variant associated with vertebral abnormality and spinal muscular atrophy with lower extremity predominance. *Pediatr Neurol* 52:239–244.
58. Scoto M, et al. (2015) Novel mutations expand the clinical spectrum of DYNC1H1-associated spinal muscular atrophy. *Neurology* 84:668–679.
59. Puls I, et al. (2001) Mutant dynactin in motor neuron disease. *Nat Genet* 33:455–456.
60. Strickland AV, et al. (2015) Mutation screen reveals novel variants and expands the phenotypes associated with DYNC1H1. *J Neurol* 262:2124–2134.
61. Mullins MC, Hammerschmidt M, Haffter P, Nüsslein-Volhard C (1994) Large-scale mutagenesis in the zebrafish: In search of genes controlling development in a vertebrate. *Curr Biol* 4:189–202.
62. Nechiporuk A, Finney JE, Keating MT, Johnson SL (1999) Assessment of polymorphism in zebrafish mapping strains. *Genome Res* 9:1231–1238.
63. Obholzer N, et al. (2008) Vesicular glutamate transporter 3 is required for synaptic transmission in zebrafish hair cells. *J Neurosci* 28:2110–2118.
64. Almeida RG, Czopka T, Ffrench-Constant C, Lyons DA (2011) Individual axons regulate the myelinating potential of single oligodendrocytes in vivo. *Development* 138: 4443–4450.
65. Thisse C, Thisse B (2008) High-resolution in situ hybridization to whole-mount zebrafish embryos. *Nat Protoc* 3:59–69.
66. Czopka T, Lyons DA (2011) Dissecting mechanisms of myelinated axon formation using zebrafish. *Methods Cell Biol* 105:25–62.
67. Rook MS, Lu M, Kosik KS (2000) CaMKIIalpha 3′ untranslated region-directed mRNA translocation in living neurons: Visualization by GFP linkage. *J Neurosci* 20:6385–6393.
68. Smith CJ, Morris AD, Welsh TG, Kucenas S (2014) Contact-mediated inhibition between oligodendrocyte progenitor cells and motor exit point glia establishes the spinal cord transition zone. *PLoS Biol* 12:e1001961.